

Nanoscale

Accepted Manuscript



This is an *Accepted Manuscript*, which has been through the Royal Society of Chemistry peer review process and has been accepted for publication.

Accepted Manuscripts are published online shortly after acceptance, before technical editing, formatting and proof reading. Using this free service, authors can make their results available to the community, in citable form, before we publish the edited article. We will replace this *Accepted Manuscript* with the edited and formatted *Advance Article* as soon as it is available.

You can find more information about *Accepted Manuscripts* in the [Information for Authors](#).

Please note that technical editing may introduce minor changes to the text and/or graphics, which may alter content. The journal's standard [Terms & Conditions](#) and the [Ethical guidelines](#) still apply. In no event shall the Royal Society of Chemistry be held responsible for any errors or omissions in this *Accepted Manuscript* or any consequences arising from the use of any information it contains.

ARTICLE

Nanostructured porous manganese carbonate spheres with capacitive effects on the high lithium storage capability

Cite this: DOI: 10.1039/x0xx00000x

Wenpei Kang^{a,b}, Denis Yau Wai Yu^{a,c}, Wenye Li^{d,a,b}, Zhenyu Zhang^{a,b}, Xia Yang^{a,b}, Tsz-Wai Ng^{a,b}, Rujia Zou^{a,b}, Yongbing Tang^{d,a*}, Wenjun Zhang^{a,b} and Chun-Sing Lee^{a,b*}Received xxxx 2015,
Accepted xxxx 2015

DOI: 10.1039/x0xx00000x

www.rsc.org/Nanoscale

In this paper, nanostructured porous MnCO₃ spheres are facilely synthesized, which can simultaneously provide an increased surface for conversion reaction and capacitive storage as anode material of lithium ion battery. This material gives superior specific capacity and excellent long-term cycling performance even at a high current density. It can deliver a stable capacity of 1049 mAh g⁻¹ after 200 cycles at a current density of 1000 mA g⁻¹, which is much higher than theoretical capacity of 466 mAh g⁻¹. After 2000 cycles at high current of 5000 mA g⁻¹, a capacity of 510 mAh g⁻¹ can still be maintained. The high rating performance at 5000 mA g⁻¹ is among the best-reported anode materials. From the *in-situ* or *ex-situ* SEM observation, the porous MnCO₃ nanostructure can provide a stable template for reversible lithium insertion and extraction without significant morphology change and accommodate the volume change during the charge-discharge process. Also this structure increases the capacitive contribution to the total capacity compared with other MnCO₃ samples.

1. Introduction

Various applications from mobile electronic devices to electric vehicles have posed increasing demands for high-performance lithium ion batteries (LIBs).¹⁻³ Tremendous efforts have been put on developing improved electrode materials.⁴⁻¹⁵ Due to their high theoretical capacities, transition metal compounds have attracted considerable attention for applications as anode materials.^{4,9-16} Aragón et al. and Zhong et al. have shown that metal oxysalts such as carbonates have better capacities and stabilities than their corresponding oxides.^{16,24} Several recent reports have demonstrated the good potential of metal carbonate anode materials.¹⁷⁻³⁰ In particular, Zhou et al. recently reported a MnCO₃/graphene composite with a capacity of 1050 mAh g⁻¹ after 1100 cycles 2000 mA g⁻¹ and a CoCO₃-graphene composite with a capacity of 930 mAh g⁻¹ after 40 cycles at 50 mA g⁻¹.^{26,28}

Mirhashemihaghighiet et al. have pointed out that the outstanding capacity of MnCO₃ is in fact contributed by both conventional conversion reaction with lithium as well as capacitive effects as in the case of TiO₂.^{23,31} On the other hand, Su et al considered that the carbonate group contributes to the capacity via a reversible conversion between C⁴⁺ and C catalyzed by the transition metal.²⁶ The exact causes for the high capacities of metal carbonates are still controversial. To fully exploit the potential of these metal carbonates, it is thus important to carry out further systematic studies on their charge-discharge mechanisms.

In this work, we report a simple solvothermal approach for preparing porous MnCO₃ nanospheres with high performance

as LIB anode. To explore its charge-discharge mechanisms, we studied the effects of specific surface area on the performance of the MnCO₃. In addition to traditional X-ray diffraction (XRD) and X-ray photoelectron spectroscopy (XPS) measurements, we also carried out *in-situ* transmission electron microscopy (TEM) to observe the charging and discharging processes in real-time. The capacity of MnCO₃ was found to depend strongly on the specific surface area confirming the important contribution from capacitive effects. A MnCO₃ porous nanosphere sample was found to show a stable capacities of >1000 mAh g⁻¹ at a high current density of 1000 mA g⁻¹ after 200 cycles, and a capacity of ~510 mAh g⁻¹ after 2000 cycles even at a higher current density of 5000 mA g⁻¹. The stable high-rating performance at 5000 mA g⁻¹ is among the best-reported anode materials (Table S1).

2. Experimental

2.1. Preparation of nanostructured porous MnCO₃

All the reagents were used as received. To make porous MnCO₃ (p-MnCO₃), 1.0 mmol MnSO₄·4H₂O, 0.1 g polyvinylpyrrolidone (PVP) and 1.0 mmol ascorbic acid were first dissolved into a mixed solvent of 15.0 ml of water and 15.0 mL of triethylene glycol (TEG). After that, 15.0 mmol of NH₄HCO₃ was added into the above transparent solution. Subsequently, the solution was transferred into a Teflon-lined stainless steel autoclave and maintained at 180°C for 12 h. After the autoclave was cooled to room temperature naturally,

precipitated precursor was collected by centrifugation, washed several times with deionized water and ethanol, and freeze-dried. Four reference samples were also tested in the study: one synthesized with the same method without ascorbic acid (MnCO₃-R1), one synthesized with the same method without PVP (MnCO₃-R2); one synthesized with neither ascorbic acid nor PVP in a hydrothermal condition (MnCO₃-R3), and the last one is a commercial material (MnCO₃-R4).

2.2 Materials characterization

XRD measurements were carried out on a Siemens D-500 diffractometer with Cu K α radiation. SEM and TEM were respectively carried out with a Philips XL30 FEG SEM (operated at 15 kV) and a Philips FEG TEM CM200 (operated at 200 kV). *In-situ* electrochemical charge-discharge were carried out using a transmission electron microscope-scanning tunnelling microscope (TEM-STM) holder (commercialized by Nanofactory Instruments AB, Göteborg, Sweden) within a 200 kV high-resolution TEM (JEM-2100F) with beam-blank irradiation in low illumination. X-ray photoelectron spectroscopy (XPS) analysis was performed in a VG ESCALAB 220i-XL UHV surface analysis system with a monochromatic Al K α X-ray source (1486.6 eV). The specific surface areas of the samples were determined using the Brunauer-Emmett-Teller (BET) method by nitrogen adsorption/desorption measurements with a Quantachrome NOVA-3000 system at 77 K. Thermogravimetric analyzer (TGA) measurement was performed under air atmosphere with a heating step of 10 °C min⁻¹ from room temperature to 600 °C.

2.3 Electrochemical measurements

Working electrodes were prepared by mixing the as-prepared p-MnCO₃ sample with acetylene black and sodium alginate at a weight ratio of 6:2:2. LiPF₆ solution (1 mol L⁻¹) in a 1:1 (vol.) mixture of ethylene carbonate (EC) and dimethyl carbonate mixture (DMC) was used as the electrolyte. Galvanostatic cycling tests were measured using a Maccos Instruments system. Cyclic voltammetry (CV) measurements were carried out over a potential window of 0.01-3.0 V at a scan rate of 0.05 mV s⁻¹ using an electrochemical workstation (CHI 660D).

3. Results and Discussion

Mono-dispersed porous MnCO₃ spheres were easily obtained through the mentioned simple solvothermal process without further heat treatment. Fig. 1a shows an XRD pattern of the porous MnCO₃ nanospheres (p-MnCO₃) which matches well to the standard XRD patterns of MnCO₃ with a hexagonal-rhombohedral structure (JCPDS No. 86-0173). There is no observable impurity in the obtained samples. The unit cell of crystalline MnCO₃ is shown in Fig. 1b, consisting of MnO₆ octahedra with CO₃ equilateral triangles arranged in the same plane perpendicular to the z-axis. XRD patterns of the other reference samples are the same.

Oxidation states of the chemical elements in the p-MnCO₃ sample were further investigated using XPS. A survey spectrum (Fig. 1c) shows the presence of Mn, O and C with no observable impurity. A Mn 2p core-level spectrum (Fig. 1d) shows two major peaks with binding energies at 639.8 and 651.9 eV with a separation of 12.1 eV. These peaks are assigned to Mn 2p_{3/2} and Mn 2p_{1/2}, respectively, which coincide with Mn

in the 2⁺ state.^{32,33} The carbonate group (CO₃²⁻) is confirmed by the C 1s peak at a binding energy of 289.1 eV (Fig. 1e) and the O 1s core level at 530.4 eV, as shown in Fig. 1f.^{33,34} The C 1s peak at 285.2 eV is attributed to carbon residuals on the surface of the material during the decomposition of PVP and ascorbic acid.

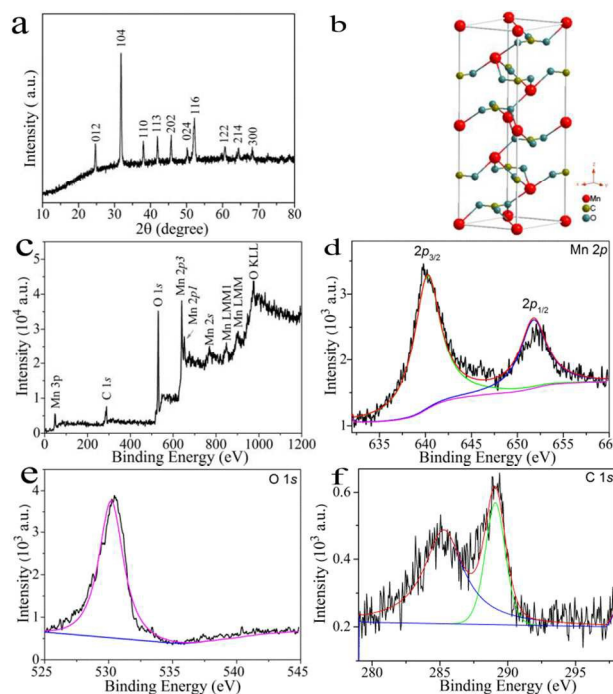


Fig. 1 (a) XRD pattern and (b) crystal structure of MnCO₃; XPS spectra of the p-MnCO₃ nanostructure: (c) a survey spectrum, (d) a Mn 2p, (e) a C 1s and (f) a O 1s core level spectra.

SEM images (Fig. 2a, b) show that the p-MnCO₃ sample consists of mono-dispersed spheres with a diameter of about 500 nm. The same information can be obtained from a low-resolution TEM image (Fig. 2c). It is clear from Fig. 2b that the spheres are made up of smaller nanoparticles and a TEM image in Fig. 2d shows that the spheres are porous inside. A selected area electron diffraction (SAED) pattern (Fig. 2e) from the sphere in the middle of Fig. 2d show that the sphere is a polycrystalline assembly of crystallites. Fig. 2f is an HR TEM image taken from one crystallite on the surface of the sphere. Lattice fringes with interplanar spacings of 0.352 and 0.234 nm, corresponding respectively to the (012) and the (110) planes of rhombohedral MnCO₃. In comparison, the reference MnCO₃ synthesized without ascorbic acid (MnCO₃-R1) or without PVP (MnCO₃-R2) shows particles with irregular shapes (Fig. S1c and d) and the sample synthesized with neither ascorbic acid nor PVP in a hydrothermal reaction (MnCO₃-R3) shows smooth solid particles with much larger diameters of about 2 μ m (Fig. S1b). This suggests that the additives are essential for forming the uniform porous spheres at nanometer sizes.

TGA was also carried out to estimate the thermal stability of the p-MnCO₃ and the result is shown in Fig. S2. The material starts to disintegrate at about 280 °C and completely decomposes at around 400 °C with a total weight loss of 37.0%, indicating it is stable below 280 °C. BET analysis of porous MnCO₃ gives a specific surface area of 25.4 m² g⁻¹, a pore volume of 0.188 cm³ g⁻¹ and an average pore diameter of 3.2

nm (Fig. S3a). In comparison, the micro-size solid particle ($\text{MnCO}_3\text{-R3}$) and the commercial sample ($\text{MnCO}_3\text{-R4}$) has BET areas of 17.2 and 11.3 $\text{m}^2 \text{g}^{-1}$ (Fig. S3b, c), respectively. The three samples were used for investigating the effects of surface contributions to the Li storage capacity.

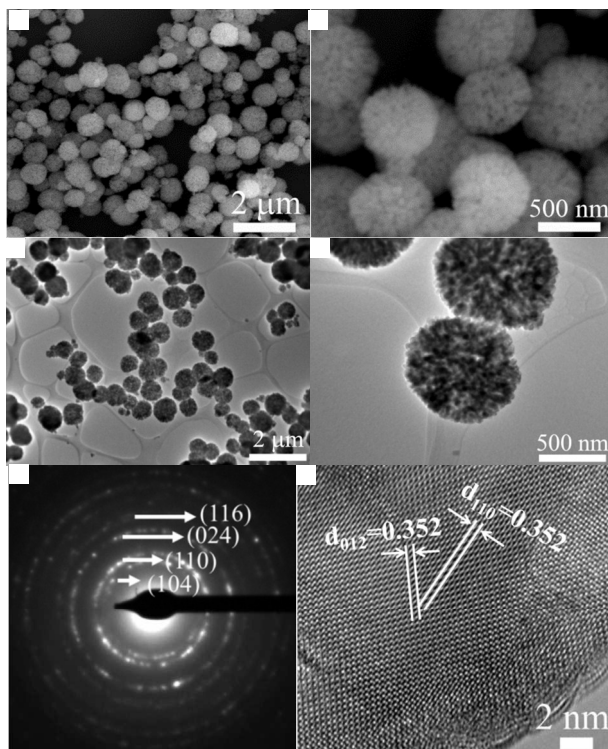


Fig. 2 (a, b) SEM images, (c, d) TEM images, (e) SAED pattern and (f) HR TEM image of the nanostructured porous MnCO_3 .

The p- MnCO_3 material is made into electrodes and tested with a Li counter electrode to investigate its electrochemical lithium-storage properties. Fig. 3a shows the first three cyclic voltamograms (CV) of the p- MnCO_3 electrode at a scanning rate of 0.05 mV s^{-1} between 0-3.0 V. Two sharp reduction peaks located at ~ 0.38 and 0.08 V during the first cycle were observed, which are attributed to solid electrolyte interphase (SEI) formation and reduction of MnCO_3 to Mn, respectively.³⁵ A broad peak between 0.5 and 1.7 V during the first anodic scan is ascribed to the oxidation of Mn to Mn^{2+} . In subsequent cycles, only one strong reduction peak at 0.32 V was observed, while there is little change to the oxidation peak. Fig. 3b shows typical discharge/charge profiles of the LIB with p- MnCO_3 over the voltage range of 0.01-3.0 V. An activation process during the first discharge, commonly seen for conversion materials, was observed at 0.25V. The discharge plateau becomes ~ 0.5 V in the following cycles, which is lower than that of other transition metal compounds.³⁶⁻³⁸ The initial discharge capacity is 1895 mAh g^{-1} with a first cycle efficiency of 65.4%. The capacity loss during the first cycle is mainly attributed to the formation of SEI during the first discharge process as shown in the CV result.³⁹ The charge-discharge capacity was found to be a function of surface area. The capacities of p- MnCO_3 , micro-sphere ($\text{MnCO}_3\text{-R2}$) and commercial materials ($\text{MnCO}_3\text{-R3}$) at a current rate of 100 mA g^{-1} are 1331, 710 and 568 mAh g^{-1} , respectively (Fig. S4). All of them are higher than the theoretical capacity of 466 mAh g^{-1} assuming two electron transfers. These results also show that

the higher the surface area, the larger is the available capacity (Fig. 3c), suggesting surface contributions to the capacity. The charge-discharge mechanism will be further discussed in the next section.

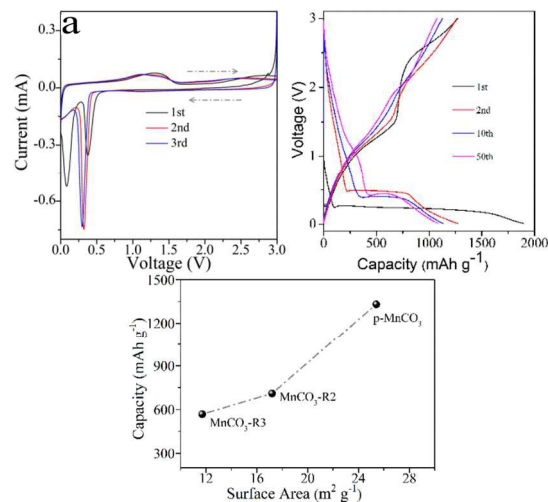


Fig. 3 (a) CV curves at a scan rate of 0.05 mV s^{-1} over the voltage range of 0-3.0 V and (b) Representative charge-discharge curves of the electrode with the spherical porous MnCO_3 particles; (c) Relationship between capacity at a current density of 100 mA g^{-1} and specific surface area of various MnCO_3 samples.

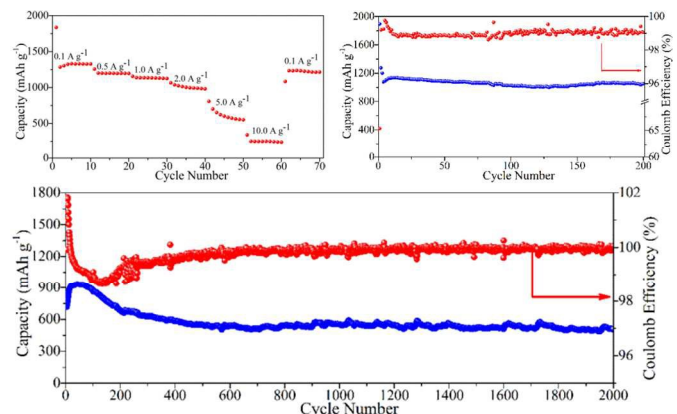


Fig. 4 (a) Rate capability, (b) Cycling performance at current density of 1000 mA g^{-1} , and (c) long-term cycling at a high current density of 5000 mA g^{-1} for p- MnCO_3 after initial 3 cycles at a current density of 100 mA g^{-1} .

The p- MnCO_3 sphere electrode exhibits excellent rate and cycle performances (Fig. 4). Upon cycling at current densities of 100, 500, 1000, 2000, 5000 and 10000 mA g^{-1} , the porous MnCO_3 electrode deliver discharge capacities of 1284, 1200, 1138, 1038, 700 and 252 mAh g^{-1} , respectively. The capacity is recovered to 1234 mAh g^{-1} when the current density is reduced back to 100 mA g^{-1} , indicating the material has good cycle stability. Long-term cycling performance of the p- MnCO_3 electrode was also measured at high current densities of 1000 mA g^{-1} and 5000 mA g^{-1} (Fig. 4b, 4c). At a current density of 1000 mA g^{-1} , after several cycles of activation with a slight increase in capacity initially, the discharge capacity settles down to ~ 1049 mAh g^{-1} with cycle efficiency around ~ 99 %. Even at a current rate of 5000 mA g^{-1} , the material can

maintain a stability capacity of $\sim 510 \text{ mAh g}^{-1}$ after 2000 cycles (as shown in Fig. 4c). Our porous MnCO_3 material not only exhibits better rate capability and cycle stability compared with other transition metal oxysalt anodes reported in the literature (Table S2), its performance at high ratings is also comparable with the state-of-the-art anode materials (Table S1).

To further understand the causes of the high stability of the p- MnCO_3 nanosphere, its morphology changes upon cycling were studied (Fig. 5). SEM and TEM images of the electrode after 1 (Fig. 5a and 5b) and 200 (Fig. 5c, 5d and 5e) cycles show that the active material maintains its original size and porous nanostructure. An HRTEM image of the cycled sample (Fig. 5f) shows a surface layer (marked by two white curves) and some small nano-crystal grains (circled by white rings). The surface layer is probably from the SEI formation. On the other hand, the material maintains its overall morphologies and this contributes to the good cycle stability of the material.

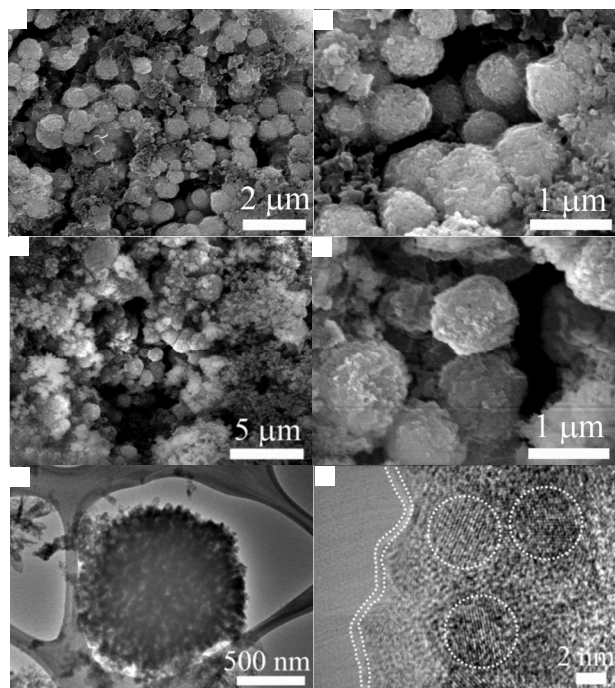


Fig. 5 SEM images of the porous MnCO_3 observed after (a, b) 1 cycle and (c, d) 200 cycles; (e, f) TEM images after 200 cycles at current density of 1000 mA g^{-1} .

In-situ TEM experiment was carried out to investigate the structural stability of the p- MnCO_3 sample during Li insertion and extraction using a dual-probe biasing TEM holder.^{40,41} MnCO_3 spheres were decorated on a Cu wire probe, and a small piece of Li metal with a Li_2O surface layer was attached to the tip of the opposite tungsten wire probe. By manipulating a piezoelectric motor on the TEM holder, a MnCO_3 sphere is in contact with the lithium metal, and a bias voltage of -3.0 V was applied to drive Li ions through the Li_2O solid-state electrolyte. During lithiation, the small nanocrystals in the MnCO_3 sphere expand and occupy the void spaces, but little change to the overall spherical structure was observed (Fig. 6a). During delithiation, again, no significant change to the morphology of the sphere was observed during lithium extraction (Fig. 6b). The observations suggest that the porous structure allows effective charge transfer, keeps the particles in place and accommodates the volume changes during charge and discharge, as shown in a schematic diagram in Fig. 6c.

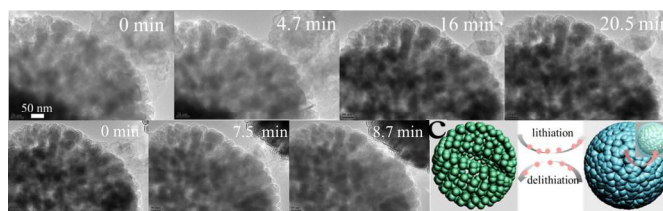


Fig. 6 *In-situ* TEM images following morphologic changes of one porous MnCO_3 sphere upon (a) lithiation and (b) delithiation for different durations (white labels on top right hand corner of each figure); (c) Schematic diagram for the structure changes of a porous MnCO_3 sphere during the lithiation and delithiation process.

In general, the total stored charge in a transition metal compound anode can be separated into two parts: (1) a faradic contribution based on the conversion reaction with lithium and (2) a complex process involving both pseudo-capacitive contribution (surface intercalation) and capacitive contribution (double-layer effect).²⁹

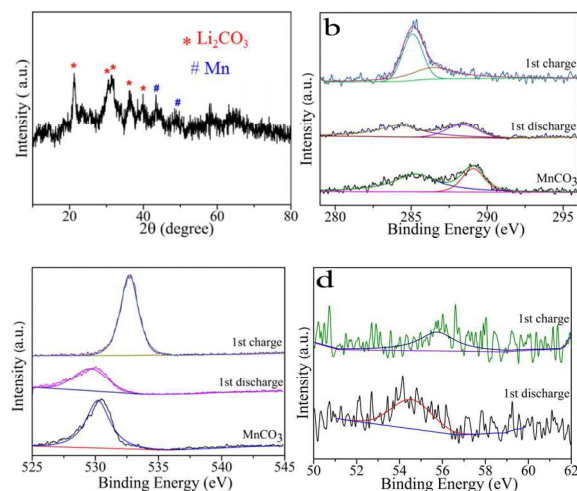
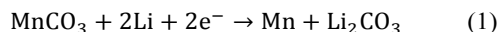


Fig. 7 (a) XRD pattern of the p- MnCO_3 electrode after first discharge; XPS spectra for the p- MnCO_3 electrode at different discharge-charge stage: (b) C 1s (c) O 1s and (d) Li 1s core level spectra.

The conversion reaction of MnCO_3 can be described by Eq. 1, with a theoretical capacity of 466 mAh g^{-1} . XRD and XPS were used to elucidate the actual reaction mechanism. Fig. 7a shows an XRD pattern of the p- MnCO_3 electrode materials after the first discharge process and subsequent removing of the electrolyte, binder etc. by rinsing with acetone. Mn and Li_2CO_3 peaks were observed after full lithiation, showing complete reaction of MnCO_3 with Li during first discharge, as in Eq. 1. An XRD pattern of the electrode after the first charge process shows no obvious peak (and thus not shown here), suggesting that the material is amorphous upon lithium removal. Results from XPS core level spectra (C 1s, O 1s, Li 1s) of the sample after the first discharge and charge stages are shown in Fig. 7b, 7c and 7d. After the discharge, the peaks for the C1s, O1s are close to their corresponding peaks in MnCO_3 , indicating the existence of CO_3^{2-} originated from the Li_2CO_3 .⁴²⁻⁴⁴ However, the C 1s and O 1s profiles changed considerably

upon delithiation, suggesting that crystalline MnCO_3 is not recovered after removal of Li^+ ions. This is consistent with electron paramagnetic resonance results obtained by Tirado's group.²⁰

The conversion reaction from Eq. 1 can only give a capacity of 466 mAh g^{-1} . Tirado suggested that the extra capacity is originated from a capacitive contribution. To verify that, a symmetric supercapacitor with two identical p- MnCO_3 electrodes was tested with CV at a scan rate of 50 mV s^{-1} (Fig. S5). The rectangular shape of the CV curve indicates electric double layer performance, in support of the capacitive contribution to the capacity of p- MnCO_3 anode in lithium-ion battery. In addition, specific capacity of MnCO_3 samples with different specific surface areas are compared (porous MnCO_3 , micro-sphere MnCO_3 and commercial MnCO_3) (Fig. S4), and the results show that capacity scales with BET surface area (Fig. 3c). This also indicates that the extra capacity comes from surface contribution. Overall, the capacity from MnCO_3 is attributed to both conversion reaction and surface capacitive storage. The present porous MnCO_3 material gives improved capacity and cyclability as anode materials for lithium-ion battery.

4. Conclusions

Nanostructured porous MnCO_3 spheres can be obtained through a one-step solvothermal reaction. The material shows superior stable capacity as anode for lithium-ion battery. At current densities of 1000 mA g^{-1} and 5000 mA g^{-1} , stable discharge capacities of $\sim 1049 \text{ mAh g}^{-1}$ after 200 cycles and 510 mAh g^{-1} after 2000 cycles, respectively, are obtained. The high capacity obtained from p- MnCO_3 is the result of conversion reaction with Mn/Mn^{2+} and capacitive contribution from the surface of the material. The larger the surface area, the higher is the available capacity. The excellent rate performance is attributed to the porous sphere structures, which allows fast lithium ion diffusion. *In-situ* TEM and *ex-situ* SEM observations also show that the structure is maintained during the lithiation-delithiation process, enabling a stable capacity during long-term cycling.

Acknowledgements

This project has been financially supported by National Natural Science Foundation of China (Nos. 51272217, 51302238), Guangdong Innovative and Entrepreneurial Research Team Program (No. 2013C090).

Notes and references

a Center of Super-Diamond and Advanced Films (COSDAF), City University of Hong Kong, Hong Kong SAR, People's Republic of China.

b Department of Physics and Materials Science, City University of Hong Kong, Hong Kong SAR, People's Republic of China.

c School of Energy and Environment, City University of Hong Kong, Hong Kong SAR, People's Republic of China.

d Functional Thin Films Research Center, Shenzhen Institutes of Advanced Technology, Chinese Academy of Sciences, People's Republic of China.

E-mail: tangyb@siat.ac.cn; apcslee@cityu.edu.hk; Tel: +852-34427826

Electronic Supplementary Information (ESI) available: [details of any supplementary information available should be included here]. See DOI: 10.1039/b000000x/

- M. V. Reddy, G. V. Subba Rao, B. V. R. Chowdari, *Chem. Rev.*, 2013, **113**, 5364-5457.
- L. G. Lu, X. B. Han, J. Q. Li, J. F. Hua, M. G. Ouyang, *J. Power Sources*, 2013, **226**, 272-288.
- J. Liu, J. G. Zhang, Z. G. Yang, J. P. Lemmon, C. Imhoff, G. L. Graff, L. Y. Li, J. Z. Hu, C. M. Wang, J. Xiao, G. Xia, V. V. Viswanathan, S. Baskaran, V. Sprenkle, X. L. Li, Y. Y. Shao, B. Schwenzer, *Adv. Funct. Mater.*, 2013, **23**, 929-946.
- P. Poizot, S. Laruelle, S. Grugeon, L. Dupont, J. M. Tarascon, *Nature*, 2000, **407**, 496-499.
- L. W. Ji, Z. Lin, M. Alcoutlabi, X. W. Zhang, *Energy Environ. Sci.*, 2011, **4**, 2682-3699.
- Y. G. Wang, H. Q. Li, P. He, E. Hosono, H. S. Zhou, *Nanoscale*, 2010, **2**, 1294-1305.
- G. Q. Zhang, B. Y. Xia, C. Xiao, L. Yu, X. Wang, Y. Xie, X. W. Lou, *Angew Chem Int Edit*, 2013, **52**, 8643-8647.
- F. Y. Cheng, J. Liang, Z. L. Tao, *J. Chem. Adv. Mater.*, 2011, **23**, 1695-1715.
- L. Zhou, D. Y. Zhao, X. W. Lou, *Adv. Mater.*, 2012, **24**, 745-748.
- J. X. Zhu, Z. Y. Yin, D. Yang, T. Sun, H. Yu, H. E. Hoster, H. H. Hng, H. Zhang, Q. Y. Yan, *Energ. Environ. Sci.*, 2013, **6**, 987-993.
- Z. S. Wu, W. C. Ren, L. Wen, L. B. Gao, J. P. Zhao, Z. P. Chen, G. M. Zhou, F. Li, H. M. Cheng, *ACS Nano*, 2010, **4**, 3187-3194.
- X. Li, X. Meng, J. Liu, D. Geng, Y. Zhang, M. Banis, Y. Li, R. Li, X. Sun, M. Cai, M. Verbrugge, *Adv. Funct. Mater.*, 2012, **22**, 1647-1654.
- W. P. Kang, Y. B. Tang, W. Y. Li, Z. P. Li, X. Yang, J. Xu, C. S. Lee, *Nanoscale*, 2014, **6**, 6551-6556.
- J. Bai, X.G. Li, G.Z. Liu, Y.T. Qian, S.L. Xiong, *Adv. Funct. Mater.*, 2014, **24**, 3012-3020.
- L. Zhang, H. B. Wu, S. Madhavi, H. H. Hng, X. W. Lou, *J. Am. Chem. Soc.*, 2012, **134**, 17388-17391.
- R. Liu, S. Q. Zhao, M. M. Zhang, F. Feng, Q. Shen, *Chem. Commun.*, 2015, **51**, 5728-5731.
- M. J. Aragón, C. Pérez-Vicente, J. L. Tirado, *Electrochem. Commun.*, 2007, **9**, 1744-1748.
- Y. Sharma, N. Sharma, G. V. Subba Rao, B. V. R. Chowdari, *J. Mater. Chem.*, 2009, **19**, 5047-5054.
- M. C. López, J. L. Tirado, C. Pérez Vicente, *J. Power Sources*, 2013, **227**, 65-71.
- M. J. Aragón, B. León, C. P. Vicente, J. L. Tirado, *Inorg. Chem.*, 2008, **47**, 10366-10371.
- M. J. Aragón, B. León, C. P. Vicente, J. L. Tirado, *Chem. Mater.*, 2009, **21**, 1834-1840.
- S. Q. Zhao, Y. Yu, S. S. Wei, Y. X. Wang, C. H. Zhao, R. Liu, Q. Shen, *J. Power Sources*, 2014, **253**, 251-255.
- S. Mirhashemihaghighi, B. León, C. P. Vicente, J. L. Tirado, R. Stoyanova, M. Yoncheva, E. Zhecheva, R. S. Puche, E. M. Arroyo, J. R. de Paz, *Inorg. Chem.*, 2012, **51**, 5554-5560.
- Z. J. Ding, B. Yao, J. K. Feng, J. X. Zhang, *J. Mater. Chem. A*, 2013, **1**, 11200-11209.

- 25 Y. R. Zhong, L. W. Su, M. Yang, J. P. Wei, Z. Zhou, *ACS Appl. Mater. Interfaces*, 2013, **5**, 11212-11217.
- 26 L. W. Su, Z. Zhou, X. Qin, Q. W. Tang, D. H. Wu, P. W. Shen, *Nano Energy*, 2013, **2**, 276-282.
- 27 W. Kang, Q. Shen, *J. Power Sources*, 2013, 238, 203-209.
- 28 Y. R. Zhong, M. Yang, X. L. Zhou, Y. T. Luo, J. P. Wei, Z. Zhou, *Adv. Mater.*, 2015, **27**, 806-812.
- 29 B. Yao, Z. J. Ding, X. Y. Feng, L. W. Yin, Q. Shen, Y. C. Shi, J. X. Zhang, *Electrochim. Acta*, 2014, **148**, 283-290.
- 30 S. Q. Zhao, S. S. Wei, R. Liu, Y. X. Wang, Y. Yu, Q. Shen, *J. Power Sources*, 2015, **284**, 154-161.
- 31 T. Brezesinski, J. Wang, J. Polleux, B. Dunn, S. H. Tolbert, *J. Am. Chem. Soc.*, 2009, **131**, 1802-1809.
- 32 Y. M. Sun, X. L. Hu, W. Luo, F. F. Xia, Y. H. Huang, *Adv. Funct. Mater.*, 2013, **23**, 2436-2444.
- 33 J. J. Yuan, J. W. Zhu, H. P. Bi, Z. Z. Zhang, S. Chen, S. M. Liang, X. Wang, *RSC Adv.*, 2013, **3**, 4400-4407.
- 34 D. R. Her, D. L. Blanchard, M. H. Engelhard, J. M. Zachara, *Surf Interface Anal.*, 1991, **17**, 25-30.
- 35 L. Zhou, X. Kong, M. Gao, F. Lian, B. Li, Z. Zhou, H. Cao, *Inorg Chem.*, 2014, **53**, 9228-9234.
- 36 Y. Yan, Y. Zhu, Y. Yu, J. Li, T. Mei, Z. Ju, Y. T. Qian, *J Nanosci Nanotechnol.*, 2012, **12**, 7334-7338.
- 37 J. Hassoun, K. S. Lee, Y. K. Sun, B. Scrosati, *J. Am. Chem. Soc.*, 2011, **133**, 3139-3143.
- 38 Y. Yu, C. H. Chen, J. L. Shui, S. Xie, *Angew. Chem. Int. Ed.*, 2005, **44**, 7085-7089.
- 39 W. P. Kang, Y. B. Tang, W. Y. Li, X. Yang, H. T. Xue, C.S. Lee, *Nanoscale*, 2015, **7**, 225-231.
- 40 N. Liu, Z. D. Lu, J. Zha, M. T. McDowell, H. W. Lee, W. T. Zhao, Y. Cui, *Nature Nanotechnology*, 2004, **9**, 187-192.
- 41 R. J. Zou, K. B. Xu, T. Wang, G. J. He, Q. Liu, X. J. Liu, Z. Y. Zhang, J. Q. Hu, *J. Mater. Chem. A*, 2013, **1**, 8560-8566.
- 42 D. Yonekura, E. Iwama, N. Ota, M. Muramatsu, M. Saito, Y. Orikasa, W. Naoid, K. Naoi, *Phys. Chem. Chem. Phys.*, 2014, **16**, 6027-6032.
- 43 B. B. Tian, J. Świątowska, V. Maurice, S. Zanna, A. Seyeux, L. H. Klein, P. Marcus, *Langmuir*, 2014, **30**, 3538-3547.
- 44 L. Martin, H. Martinez, D. Poinot, B. Pecquenard, F. Le Cras, *J. Power Sources*, 2004, **248**, 861-873.